RAA 2015 Vol. **15** No. **8**, 1342–1363 doi: 10.1088/1674–4527/15/8/017
http://www.raa-journal.org *http://www.iop.org/journals/raa*

***R**esearch in*
***A**stronomy and*
***A**strophysics*

Galactic disk bulk motions as revealed by the LSS-GAC DR2

Ning-Chen Sun[1], Xiao-Wei Liu[1,2], Yang Huang[1], Hai-Bo Yuan[⋆2], Mao-Sheng Xiang[1], Hua-Wei Zhang[1], Bing-Qiu Chen[⋆1], Juan-Juan Ren[⋆1], Chun Wang[1], Yong Zhang[3], Yong-Hui Hou[3], Yue-Fei Wang[3] and Ming Yang[4]

[1] Department of Astronomy, Peking University, Beijing 100871, China; *sunnc.astro@pku.edu.cn; x.liu@pku.edu.cn; yanghuang@pku.edu.cn*
[2] Kavli Institute for Astronomy and Astrophysics, Peking University, Beijing 100871, China
[3] Nanjing Institute of Astronomical Optics & Technology, National Astronomical Observatories, Chinese Academy of Sciences, Nanjing 210042, China
[4] Key Laboratory of Optical Astronomy, National Astronomical Observatories, Chinese Academy of Sciences, Beijing 100012, China

Abstract We report a detailed investigation of the bulk motions of the nearby Galactic stellar disk, based on three samples selected from the LSS-GAC DR2: a global sample containing 0.57 million FGK dwarfs out to $\sim$2 kpc, a local subset of the global sample consisting of $\sim$5400 stars within 150 pc, and an anti-center sample containing $\sim$4400 AFGK dwarfs and red clump stars within windows a few degrees wide centered on the Galactic Anti-center. The global sample is used to construct a three-dimensional map of bulk motions of the Galactic disk from the solar vicinity out to $\sim$2 kpc with a spatial resolution of $\sim$250 pc. Typical values of the radial and vertical components of bulk motion range from -15 km s^{-1} to 15 km s^{-1}; in contrast, the lag behind the circular motion dominates the azimuthal component by up to $\sim$15 km s^{-1}. The map reveals spatially coherent, kpc-scale stellar flows in the disk, with typical velocities of a few tens of km s^{-1}. Bending- and breathing-mode perturbations are clearly visible, and vary smoothly across the disk plane. Our data also reveal higher-order perturbations, such as breaks and ripples, in the profiles of vertical motion versus height. From the local sample, we find that stars from different populations exhibit very different patterns of bulk motion. Finally, the anti-center sample reveals a number of peaks in stellar number density in the line-of-sight velocity versus distance distribution, with the nearer ones apparently related to the known moving groups. The "velocity bifurcation" reported by Liu et al. at Galactocentric radii 10–11 kpc is confirmed. However, just beyond this distance, our data also reveal a new triple-peaked structure.

Key words: Galaxy: disk – Galaxy: kinematics and dynamics – Galaxy: stellar content

⋆ LAMOST Fellow

1 INTRODUCTION

The stellar velocity distributions encode the assembly history and structural information about the Milky Way. The Milky Way is often approximately considered to be steady and axisymmetric. In such a model, disk stars are expected to have quite smooth and single-peaked velocity distributions, without significant bulk motions in either the radial or vertical directions (see e.g. Schwarzschild & Villiger 1907; Schönrich & Binney 2012).

This simple picture is, however, challenged by the recent detections of significant bulk motions in the nearby stellar disk. Using $\sim 1\times10^4$ stars from the Sloan Extension for Galactic Understanding and Exploration survey (SEGUE; Yanny et al. 2009), Widrow et al. (2012) determine the vertical bulk motions as a function of height from the disk mid-plane. Their results reveal wave-like perturbations and some differences in bulk motion between blue and red stars. Williams et al. (2013) report the bulk motions of $\sim 7\times10^4$ red clump (RC) stars selected from the Radial Velocity Experiment (RAVE; Steinmetz et al. 2006). They find a north-south asymmetry both in the radial and vertical bulk motions; and curiously, the vertical bulk motions exhibit some compression and rarefaction patterns across the disk. North-south asymmetry and compression patterns are also observed by Carlin et al. (2013) with $\sim 4\times10^5$ F-type stars selected from the LAMOST Galactic spectroscopic surveys (Cui et al. 2012; Zhao et al. 2012; Liu et al. 2015) and RAVE. Bovy et al. (2015) report fluctuations in differences between the observed and predicted stellar velocity distributions on scales ranging from 25 pc to 10 kpc, using data from the Apache Point Observatory Galactic Evolution Experiment (APOGEE; Eisenstein et al. 2011), RAVE and the Geneva-Copenhagen Survey (GCS; Nordström et al. 2004). They attribute the fluctuations to the effects of the central bar. In addition, Liu et al. (2012) reveal a feature of "velocity bifurcation" at Galactocentric radii 10–11 kpc with $\sim$700 RC stars in the direction of the Galactic Anti-center, and interpret it as a resonance feature of the central bar. Theoretically, Siebert et al. (2011), Debattista (2014) and Faure et al. (2014) show that bulk motions can be excited by spiral arms, and Widrow et al. (2014) investigate the dynamical effects of a passing satellite or dark matter subhalo.

By June 2014, the LAMOST Spectroscopic Survey of the Galactic Anti-Center (LSS-GAC; Liu et al. 2014; Yuan et al. 2015) had obtained spectra with S/N (4650Å) ≥ 10 for over one million stars. The second data release (DR2) of value-added catalogs provided their line-of-sight radial velocities, stellar atmospheric parameters, three-dimensional extinctions, distances and proper motions. In this paper, we report an investigation of bulk motions based on three samples selected from the LSS-GAC DR2: A global, a local and an anti-center sample. The global sample, containing $\sim$0.57 million FGK dwarfs, is used to obtain a three-dimensional map of bulk motions in the Galactic disk from the solar neighborhood out to $\sim$2 kpc with a resolution of $\sim$250 pc. The second sample, a subset of the global one, contains $\sim$5400 stars within 150 pc; we use it to investigate the bulk motions of different stellar populations in the solar neighborhood. Finally, we investigate whether the "velocity bifurcation" reported by Liu et al. (2012) is a localized structure via an analysis of the line-of-sight radial velocities of the anti-center sample, consisting of $\sim$4400 AFGK dwarfs and RC giants, tracing a contiguous distance range of 4 kpc in the Galactic Anti-center direction. The paper is organized as follows. After a description of the data in Section 2, we present results based on the three samples in Sections 3–5 in turn. We then close with a brief summary in Section 6.

2 DATA

2.1 LSS-GAC

Data used in this work are from the LSS-GAC DR2 (Xiang et al. 2015b, in preparation). LSS-GAC – the LAMOST Spectroscopic Survey of the Galactic Anti-Center (Liu et al. 2014; Yuan et al. 2015) surveys a 3400 deg^2 contiguous area centered on the Galactic Anti-center ($150^\circ < l < 210^\circ$, $-30^\circ < b < 30^\circ$) and aims to obtain optical ($\lambda\lambda$ 3700 $-$ 9000), low-resolution ($R \sim$1800) spectra

for a statistically complete sample[1] containing ∼3 million stars of all colors and magnitudes ranging from r = 14.0 to 17.8 mag (down to 18.5 mag for a limited number of fields). Over 1.5 million stars in the range $-10^\circ <$ Dec $< 60^\circ$ and brighter than r = 14 mag are also selected with a similar selection algorithm and observed under bright lunar conditions. LSS-GAC also contains a sub-program, targeting various types of objects in the M31-M33 region. By June, 2014, LSS-GAC had obtained over two million spectra with a signal-to-noise ratio at 4650 Å, S/N (4650Å) $\geq$ 10.

Line-of-sight radial velocities, V_r, and stellar atmospheric parameters (effective temperature $T_{\rm eff}$, surface gravity log g and metallicity [Fe/H]) are estimated with the LAMOST Stellar Parameter Pipeline at Peking University (LSP3; Xiang et al. 2015). For S/N (4650Å) $\geq$ 10, LSP3 has achieved accuracies better than 5.0 km s^{-1}, 150 K, 0.25 dex and 0.15 dex for V_r, $T_{\rm eff}$, log g and [Fe/H], respectively. Values of the interstellar extinction, with typical errors of ∼0.04 mag, are obtained for individual stars with the standard pairing technique (Stecher 1965, Massa et al. 1983, Yuan et al. 2013). Distances have been derived based on an empirical relation between absolute magnitudes (g_0, r_0, J_0, H_0, K_{s0}) and stellar atmospheric parameters ($T_{\rm eff}$, log g, [Fe/H]). Typical distance uncertainties are 10%–15% for dwarfs and 20%–30% for giants.

Proper motions, $\mu_\alpha \cos\delta$ and μ_δ, are from the UCAC4 (Zacharias et al. 2013) and PPMXL (Roeser et al. 2010) catalogs. UCAC4 is an all-sky, astrometric catalog containing over 113 million objects complete to R ∼16 mag. More than 105 million stars in UCAC4 have proper motions, with typical random errors of 4 mas yr^{-1}. Compiled based on USNO-B1.0, 2MASS and a previous version of PPMX, PPMXL contains over 900 million sources down to V = 20 mag. Almost all of them have proper motions, with typical random errors ranging from 4 to more than 10 mas yr^{-1}. The position-dependent systematic errors of proper motions of UCAC4 and PPMXL have been corrected by Huang et al. (2015a) and Carlin et al. (2013), respectively, using ∼1700 or ∼10^5 quasars as anchors. After the corrections, however, some unaccounted for color- and magnitude-dependent systematic errors remain, which are further discussed in Section 3.2.

2.2 Coordinate Systems and Galactic Parameters

We use two sets of coordinate systems in this paper: (a) A right-handed Cartesian coordinate system (X, Y, Z) centered on the Sun, with X increasing towards the Galactic center, Y in the direction of Galactic rotation and Z the height from the disk mid-plane, positive towards the north Galactic pole; (b) A Galactocentric cylindrical coordinate system (R, Φ, Z), with R the Galactocentric distance, Φ increasing in the direction of Galactic rotation and Z the same as that in the Cartesian system. We assume that the Sun has a Galactocentric distance $R_\odot$ = 8 kpc. This places the Galactic center at ($X_{\rm GC}$, $Y_{\rm GC}$, $Z_{\rm GC}$) = (8, 0, 0) kpc and the Sun at ($R_\odot$, $\Phi_\odot$, $Z_\odot$) = (8 kpc, 0°, 0 kpc). The three velocity components are denoted as (U, V, W) in the Cartesian system and (V_R, V_Φ, V_Z) in the cylindrical system. We use a flat rotation curve of V_c = 220 km s^{-1}, and solar motions ($U_\odot$, $V_\odot$, $W_\odot$) = (7.01, 10.13, 4.95) km s^{-1} (Huang et al. 2015a) relative to the Local Standard of Rest (LSR).

2.3 Samples

2.3.1 The global sample

We use a global sample of FGK dwarfs to construct a three-dimensional map of bulk motions in the Galactic disk from the solar vicinity out to ∼2 kpc. The stars are selected from the LSS-GAC DR2 by applying effective temperature and surface gravity cuts, $4200 < T_{\rm eff} < 6800$ K and $3.8 <$ log g

[1] In the sense that the sample stars are selected uniformly on the celestial sphere to given limiting magnitudes and randomly in color-magnitude diagrams, such that with due considerations of the various well-defined selection effects, the spectroscopically targeted sample stars can be used to recover the underlying photometric populations (cf. Yuan et al. 2015 for detail).

< 5.0 dex. Stars without UCAC4 or PPMXL proper motions are excluded and duplicate ones with lower spectral SNRs are removed. This leads to a sample of $\sim$0.70 million FGK dwarfs.

We derive the three-dimensional positions, (X, Y, Z) and (R, Φ, Z), and three-dimensional velocities, (U, V, W) and (V_R, V_Φ, V_Z), of individual stars from their celestial coordinates, (l, b), distances, d, line-of-sight radial velocities, V_r, and proper motions, $\mu_\alpha \cos\delta$ and μ_δ. For proper motions, both UCAC4 and PPMXL catalogs are used, yielding two independent sets of velocities for each star. We use a Monte Carlo method of error propagation to estimate the random errors of positions and velocities. This is done by randomly sampling the distance moduli, radial velocities and proper motions, assuming Gaussian random error distributions. For each realization of a given star, we calculate the position and velocity. This is repeated 1000 times to obtain their distributions. The standard deviations of the distributions are adopted as random errors of the position and velocity for the star of concern.

We then remove outliers and stars with large random errors by requiring: $-200 < V_R < 200$ km s^{-1}, $0 < V_\Phi < 400$ km s^{-1}, $-200 < V_Z < 200$ km s^{-1} and random errors in V_R, V_Φ and V_Z are no larger than 50 km s^{-1}. Velocities obtained with the UCAC4 and PPMXL proper motions should satisfy both these criteria to retain a star in the sample. This leaves $\sim$0.57 million FGK dwarfs in the final sample. The contours in Figure 1 display the sample in the ($g-r$, r) color-magnitude diagram. The sample covers a range of 10–17 mag in r-band magnitude and 0.1–1.7 mag in $g-r$ color. The spatial distributions of the stars can be found in Figure 2, which shows that the stars occupy a significant volume of the Galactic disk, spanning the region from the solar vicinity out to $\sim$2 kpc. The global sample is three-dimensionally sliced into small bins, with bin size (ΔR, $\Delta\Phi$, ΔZ) = (250 pc, 2°, 250 pc). The entire volume of Figure 2 thus contains a total of 2304 bins. Among them, 662 bins are found to contain stars, ranging from several to a few 10^4; and 252 bins have no fewer than 100 stars.

2.3.2 The local sample

A local sample of stars is selected by applying a distance cut, $d \leq 150$ pc, to the global sample. The local sample is less affected by the potential systematic errors in proper motions due to the distance cut. The sample contains 5443 FGK dwarfs, and is further divided into six populations according to their effective temperatures (F/G/K types) and metallicities (metal-rich and metal-poor). Table 1 (see Sect. 4) lists the numbers of stars, along with the effective temperature and metallicity ranges for each population.

Table 1 Bulk Motions of the Local Sample

			UCAC4 Proper Motions			PPMXL Proper Motions		
$T_{\rm eff}$ (K)	[Fe/H] (dex)	Number of stars	$\langle V_R \rangle$ (km s^{-1})	$\langle V_\Phi \rangle - 220$ (km s^{-1})	$\langle V_Z \rangle$ (km s^{-1})	$\langle V_R \rangle$ (km s^{-1})	$\langle V_\Phi \rangle - 220$ (km s^{-1})	$\langle V_Z \rangle$ (km s^{-1})
(6000, 6800)	> -0.4	92	-0.3 ± 1.1	2.2 ± 0.9	1.6 ± 0.6	1.0 ± 1.3	2.2 ± 0.8	2.4 ± 0.6
(5000, 6000)	> -0.4	2473	2.2 ± 0.2	-5.6 ± 0.2	-0.2 ± 0.1	2.0 ± 0.2	-5.7 ± 0.2	0.4 ± 0.1
(4200, 5000)	> -0.4	2581	4.3 ± 0.2	-5.6 ± 0.2	-1.8 ± 0.1	4.1 ± 0.2	-6.2 ± 0.2	-1.4 ± 0.1
(6000, 6800)	< -0.4	46	-6.6 ± 3.0	-0.6 ± 2.0	5.1 ± 0.5	-4.8 ± 3.4	-1.7 ± 1.9	4.5 ± 0.6
(5000, 6000)	< -0.4	170	-3.6 ± 1.5	-11.9 ± 1.4	1.4 ± 1.0	-3.4 ± 1.6	-14.1 ± 1.4	1.9 ± 0.9
(4200, 5000)	< -0.4	81	1.3 ± 2.2	-20.0 ± 1.9	1.8 ± 1.0	1.2 ± 2.2	-19.3 ± 2.1	1.5 ± 1.2

2.3.3 The anti-center sample

The anti-center sample consists of four populations, the GK-, F-, A-type dwarfs and RC giants. The dwarfs are selected from the LSS-GAC DR2 with the effective temperature and surface gravity cuts, $4200 < T_{\rm eff} < 6000$ K and 3.8 dex $<$ log $g < 5.0$ dex for GK-type stars, $6000 < T_{\rm eff} < 6800$ K

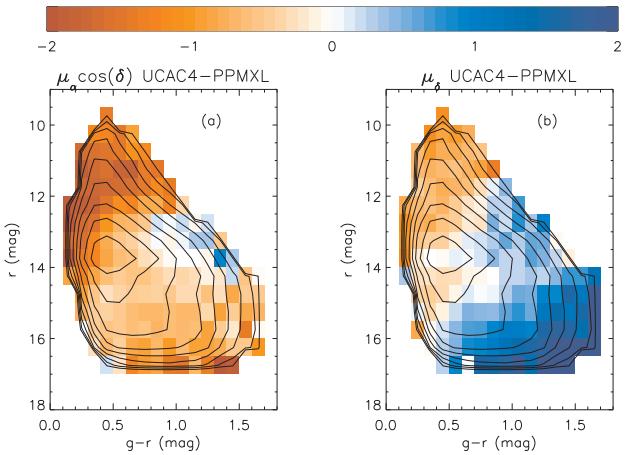

Fig. 1 Color-magnitude diagram of the global sample (contours), and the median differences between UCAC4 and PPMXL proper motions ($\mu_\alpha \cos(\delta)$ on the left and μ_δ on the right) of the member stars falling in the individual color-magnitude bins (color scale). The bins have a width of 0.1 mag in $g - r$ and 0.5 mag in r. The contours increase from 100 to $\sim 1 \times 10^4$ stars per bin with equal logarithmic steps. The color bar is in units of mas yr^{-1}.

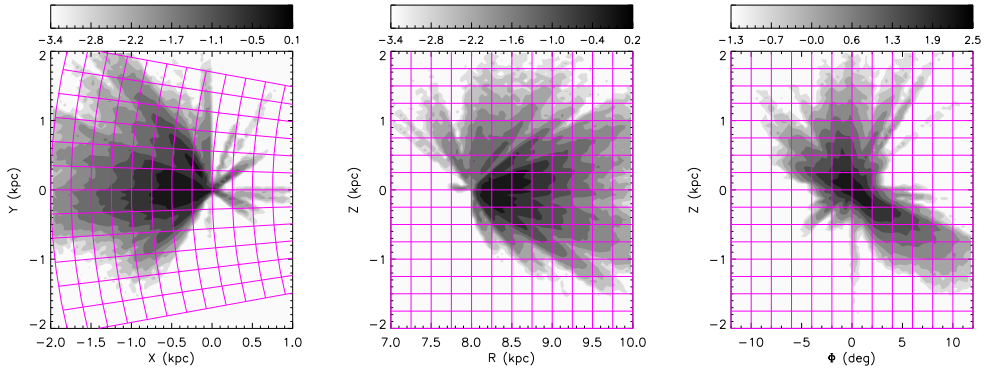

Fig. 2 Spatial distributions of the global sample. Greyscale shows the logarithmic surface density of stars in units of pc^{-2} (*left and middle panels*) or in pc^{-1} deg^{-1} (*right panel*). With spacings (ΔR, $\Delta\Phi$, ΔZ) = (250 pc, 2°, 250 pc), the magenta grids show how the sample is divided three-dimensionally when we construct the bulk motion maps.

and $3.8 < \log g < 5.0$ dex for F-type stars, and $6800 < T_{\rm eff} < 10000$ K and $3.2 < \log g < 5.0$ dex for A-type stars. The RC giants are selected by Huang et al. (2015b), as well as from the LSS-GAC DR2, based on their positions in the [Fe/H]–$T_{\rm eff}$–log g and [Fe/H]–color parameter spaces. The PARSEC stellar evolution models (Bressan et al. 2012) and high-quality asteroseismology data of *Kepler* are used to define the location of RC giants in the parameter spaces. The contamination and completeness of the selection algorithm are less than 5% and greater than 90%, respectively. RC stars are thus selected to have distance accuracies better than 5%–10%. From the chosen AFGK-type dwarfs and RC giants, we then select those falling in windows centered on the Galactic Anti-center, $|l - 180°| \leq \delta$, $|b| \leq \delta$, where δ is set to 4° for GK- and F-type dwarfs, 6° for A-type ones and 2°

for RC giants, a compromise between a sufficient number of stars (preferring a large δ) and a good alignment between the Galactocentric and line-of-sight radial velocities (preferring a small δ). The final anti-center sample contains 1716 GK-, 1402 F- and 359 A-type dwarfs and 958 RC giants. With increasing luminosities, these four populations of stars are able to trace the Galactic disk in the anti-center direction from the solar vicinity out to a Galactocentric distance of 12 kpc. The distance distributions of the anti-center sample can be found in Figure 17 (Sect. 5).

3 THE THREE-DIMENSIONAL BULK MOTION MAP

3.1 Characterizing Bulk Motions

To construct the bulk motion maps, we three-dimensionally slice the global sample into small bins (see Sect. 2.3.1 and Fig. 2).

Figure 3 displays the velocity distributions of two typical bins. The first bin has a close distance and thus less affected by the random errors that propagate from the proper motions and distances. As panel (a) shows, the distribution of V_R in the first bin shows deviations from a simple, smooth Gaussian distribution, including two peaks at -15 km s^{-1} and 10 km s^{-1}, respectively. The peaks are produced by the known moving groups (see e.g. Dehnen 1998; Antoja et al. 2012): the -15 km s^{-1} peak comes from the Sirius and Ursa Major (UMa) groups, while the one at 10 km s^{-1} is from the Pleiades and Coma Berenices groups. Deviations such as those are however not so big – a single Gaussian can still fit the overall distribution well and the median V_R finds the Gaussian peak quite precisely. A visual examination of the 252 bins with no fewer than 100 stars has found clear signatures of moving groups in the V_R profiles of only four bins, all near the Sun. Again, the presence of those moving groups hardly affects the determinations of the centroids of the distributions through the median values of V_R. Those moving groups, however, do not show up in V_Φ as obviously as in V_R of the same bin (Panel (b)). They are probably lost in the much narrower V_Φ distribution. (The moving groups have typical widths in V_R or V_Φ of $\gtrsim$ 10 km s^{-1}; see e.g. fig. 3 of Dehnen 1998.) Unlike V_R, V_Φ has long been known to skew towards lower values. This is clearly seen in the current case. Still, a single Gaussian fits the data and the median value finds the peak position well. Panel (c) shows quite a simple, single-peaked, symmetric profile of V_Z for the first bin, whose peak can be easily found by Gaussian fitting or by the median value despite the weak, extended wings at $|V_Z| \gtrsim$ 30 km s^{-1}. The second bin has a farther distance (Panels (d-f)), so large random errors that propagate from the proper motions and distances would have blurred the signatures of any moving groups, the skewness or the extended wings in the distributions of V_R, V_Φ and V_Z, respectively. In this case, the distribution profiles are well fitted by a Gaussian, whose peaks coincide well with the corresponding median values. Above all, as a first approximation, the bulk motions of stars in the individual bins can be characterized by the median values of the three components of velocity, denoted in this paper by $\langle V_R \rangle$, $\langle V_\Phi \rangle$ and $\langle V_Z \rangle$. To calculate those median values, we have required the bins to contain at least 100 stars, leaving 252 bins that are usable. The bulk motions thus derived have random errors less than $\sim$5 km s^{-1}, with typical values of $\lesssim$ 2 km s^{-1} for $\langle V_R \rangle$ and $\lesssim$ 3 km s^{-1} for $\langle V_\Phi \rangle$ and $\langle V_Z \rangle$.

3.2 Systematic Errors

3.2.1 Distances

The random errors of stellar distances do not systematically affect the bulk motions. Slightly evolved stars in the global sample, with $3.8 \leq \log g \leq 4.2$, are found to have systematically underestimated distances by $\sim$20% compared to those derived by isochrone fitting (Xiang M.-S. et al., private communications). However, the fraction of those evolved stars in our sample is small. Moreover, a $\sim$20%

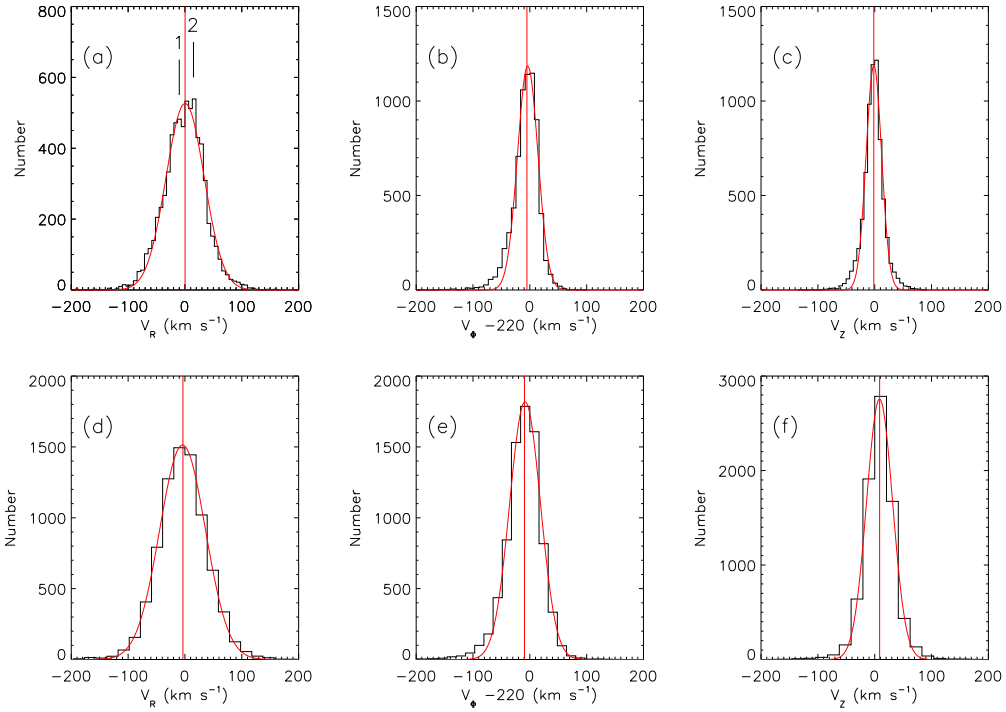

Fig. 3 Distributions of V_R (*left panels*), V_Φ (*middle panels*) and V_Z (*right panels*), derived using the UCAC4 proper motions in bins $8 < R < 8.25$ kpc, $0 < \Phi < 2^\circ$, $0 < Z < 0.25$ kpc (*upper panels*) and $8.25 < R < 8.5$ kpc, $4 < \Phi < 6^\circ$, $-0.5 < Z < -0.25$ kpc (*lower panels*). In each panel, the histogram bin size is set to be no smaller than the random errors of the 90th percentile of stars ordered by increasing error. The bin size is set in such a way to avoid artifacts introduced by the velocity errors of individual stars. The red curve is a Gaussian fit to the distribution of which the median value is marked by the red straight line. In Panel (a), Peak 1 at -15 km s^{-1} originates from the moving groups Sirius and UMa, and Peak 2 at 10 km s^{-1} comes from Pleiades and Coma Berenices.

underestimation in distances corresponds to an underestimation of the same percentage in the mean tangential velocities, which in turn contributes in a very minor way to $\langle V_R \rangle$ and $\langle V_Z \rangle$.

3.2.2 Line-of-sight radial velocities

A comparison of the line-of-sight radial velocities of stars observed by both LAMOST and APOGEE has shown that the LAMOST wavelength calibration suffers from glitches of the order of $\sim$2 km s^{-1} on a timescale of several days (Xiang M.-S. et al., private communications). The sample stars inside each bin were observed on nights ranging from typically $\sim$5 up to $\sim$60 days, with typical timespans ranging from 1–3 months to 1–3 years. We expect that the effects of those glitches largely cancel out on such a timescale, and thus hardly affect our estimates of the bulk motions. Unresolved binary stars can potentially affect the line-of-sight radial velocities due to the orbital velocities of the binary stars around their centers of mass. However, this effect is also unlikely to affect the determinations of the median velocities $\langle V_R \rangle$, $\langle V_\Phi \rangle$ and $\langle V_Z \rangle$ in a systematic way, under the reasonable assumption that the orbital orientations and phases of binary systems are randomly distributed.

3.2.3 Proper motions

The largest systematic errors affecting our results come from the proper motions, which are more significant at larger distances. The color scale in Figure 1 shows the median differences of the UCAC4 and PPMXL proper motions for the global sample. It can be seen that the differences vary systematically with $g-r$ color and r magnitude. Typical differences for $\mu_\alpha \cos\delta$ range from -1 to 0 mas yr^{-1} except for very blue or bright stars ($g-r<0.3$ mag or $r<12.5$ mag), for which the differences amount to -2 mas yr^{-1}. For μ_δ, the systematic differences typically range from -1 to 1 mas yr^{-1}; but very red or faint stars ($g-r>1.3$ mag or $r>16.0$ mag) are found to have values up to 2 mas yr^{-1}. Thus, even after being corrected for systematics using samples of distant quasars, the proper motions from UCAC4 and PPMXL still suffer from the unaccounted for color- and magnitude-dependent systematic errors. In the current work, we have used proper motions from both catalogs and deem the result robust if it is seen using both UCAC4 and PPMXL.

3.2.4 Algorithm biases

As we shall see later, $\langle V_R\rangle$, $\langle V_\Phi\rangle$ and $\langle V_Z\rangle$ all vary spatially in three dimensions, i.e. in (R, Φ, Z) or (X, Y, Z). If the bulk motions are estimated by projecting the stars to a two-dimensional plane, the results are unlikely to be a good representation of the distribution in case the bulk motions vary significantly in the projected dimension. For example, the mean V_R of stars within bin (R_1-R_2, Z_1-Z_2) is a weighted mean of $\langle V_R\rangle(\Phi|R_1-R_2, Z_1-Z_2)$ with weights $n(\Phi|R_1-R_2, Z_1-Z_2)$, where n is the stellar number density of the sample used. Samples of different n could yield quite different results. This problem is naturally avoided by three-dimensional binning, as we have done here for the global sample.

3.2.5 Selection effects

As we shall see in Section 4, different populations seem to have different bulk motions. The differences in $\langle V_R\rangle$ and $\langle V_Z\rangle$ are relatively small, i.e. on the order of a few km s^{-1}. However, $\langle V_\Phi\rangle$ has larger differences, $\sim$10 km s^{-1}, between different populations. The global sample contains stars spanning a wide range of effective temperatures and metallicities, and thus suffers from selection effects. The selection effects in $\langle V_R\rangle$ and $\langle V_Z\rangle$ are less important, compared with the systematic errors introduced by proper motions (from several to more than 10 km s^{-1}; see Figs. 4-9). In contrast, the selection effects in $\langle V_\Phi\rangle$ are expected to be more significant. We do not correct for the selection effects in the current paper.

3.2.6 The solar motions

Bovy et al. (2015) point out that bulk motions have a significant effect on the determination of solar motion with respect to the LSR. With stars spanning the regions from the solar vicinity out to $\sim$5 kpc, they determine the azimuthal component of solar motion to be $V_\odot$ $\sim$24 km s^{-1}, much larger than the previously locally-determined results. The discrepancy can be explained if the local Galactic disk has a bulk motion of $\sim$10 km s^{-1} (Bovy et al. 2015). In this paper, we have calculated stellar velocities adopting a locally-determined set of solar motions, ($U_\odot$, $V_\odot$, $W_\odot$) = (7.01, 10.13, 4.95) km s^{-1} (Huang et al. 2015a). Here we do not aim to obtain a better set of solar motions, which may well vary depending on the spatial extension of stars used to determine them in view of the finding of Bovy et al. In any case, the bulk motions, $\langle V_R\rangle$, $\langle V_\Phi\rangle$ and $\langle V_Z\rangle$, reported here can be updated in the future by simply applying the corresponding offsets, $\delta U_\odot$, $\delta V_\odot$ and $\delta W_\odot$, between the future new and the current solar motions, as we approximately have $\delta(\langle V_R\rangle - U_\odot)$, $\delta(\langle V_\Phi\rangle - V_\odot)$ and $\delta(\langle V_Z\rangle - W_\odot)$ $\sim$0 km s^{-1} for our sample.

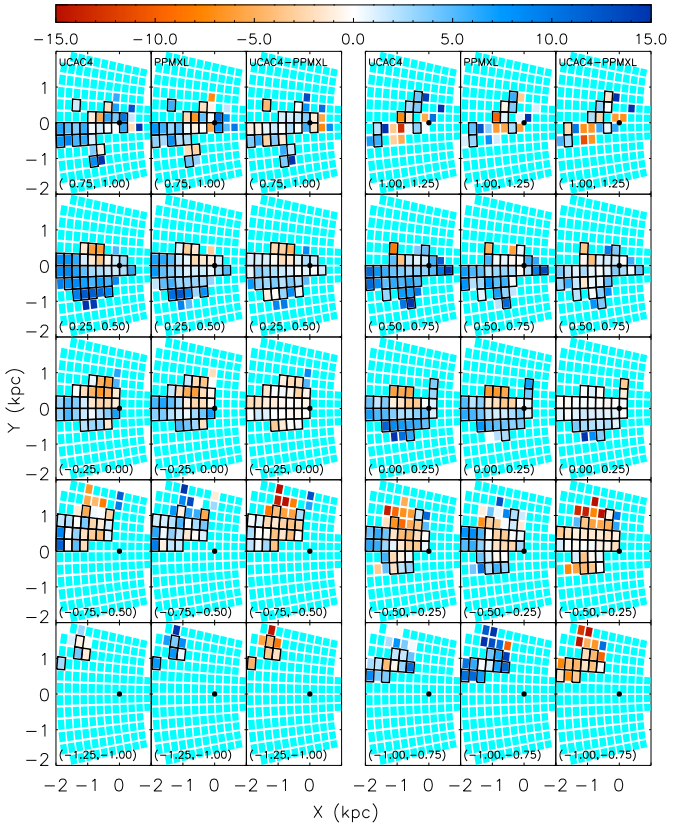

Fig. 4 Distributions of $\langle V_R \rangle$ obtained with both the UCAC4 or the PPMXL proper motions and their differences in units of km s^{-1} viewed in the X–Y plane. Boxes in black show bins where the differences are no larger than 5 km s^{-1}. Numbers in the brackets show the ranges of Z in units of kpc. The black dot denotes the location of the Sun.

3.3 The Bulk Motions

3.3.1 Radial component $\langle V_R \rangle$

Figures 4 and 5 show the maps of radial bulk motion $\langle V_R \rangle$. For most bins, the differences between the UCAC4 and PPMXL results are no larger than 5 km s^{-1}. $\langle V_R \rangle$ is clearly nonzero, but ranges from ~ -15 km s^{-1} to $\sim$15 km s^{-1}, consistent with previous studies (e.g. Williams et al. 2013; Carlin et al. 2013). Most parts of the disk that have been mapped have outward bulk motions. However, inward motions dominate a large region near the Sun, i.e. the region defined by $8 < R < 9$ kpc, $0 < \Phi < 6°$, $-0.75 < Z < 0.5$ kpc, or roughly $-1 < X < 0$ kpc, $0 < Y < 1$ kpc and $-0.75 < Z < 0.5$ kpc.

3.3.2 Azimuthal component $\langle V_\Phi \rangle$

Figures 6 and 7 show the maps of azimuthal bulk motion $\langle V_\Phi \rangle$, from which we have subtracted a constant circular motion of V_c = 220 km s^{-1} for clarity. The UCAC4 and PPMXL proper motions

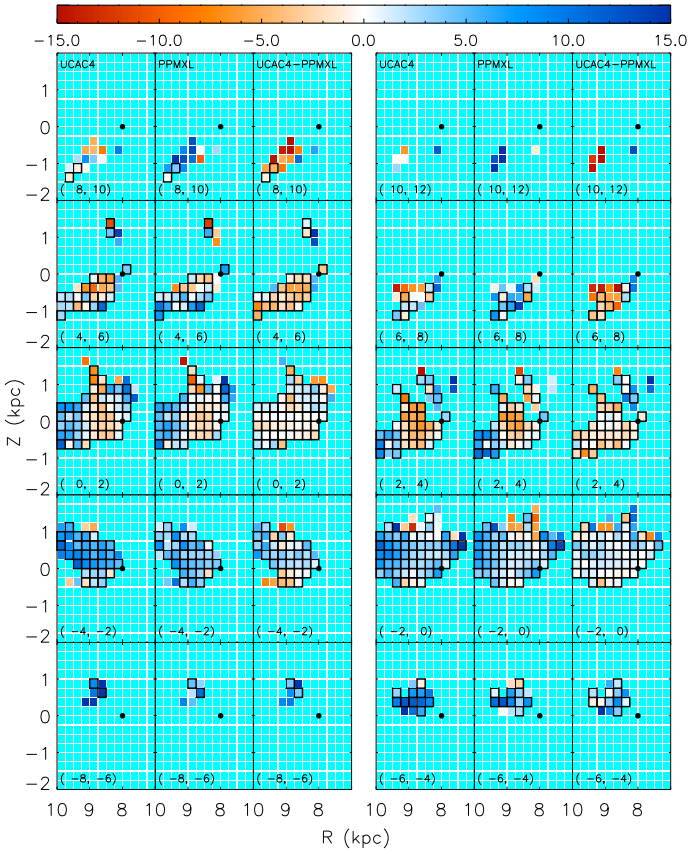

Fig. 5 Same as Fig. 4 but for the R–Z plane. Numbers in the brackets show the ranges of Φ in units of degrees.

give consistent results for most bins, with differences no larger than 5 km s^{-1}. The Galactic disk is dominated by negative values of $\langle V_\Phi \rangle - V_c$, which decrease systematically as one moves away from the mid-plane. Near $Z \sim$0 kpc, the stars lag behind the circular motion by $\sim$8 km s^{-1}; but at $|Z| \sim$1 kpc, the stars have $\langle V_\Phi \rangle - V_c \lesssim -15$ km s^{-1}. Similar trends are also unveiled by Williams et al. (2013). As mentioned in Section 3.2.5, $\langle V_\Phi \rangle$ could be affected by some selection effects. The later-type stars, which are expected to have larger asymmetric drifts, are concentrated close to the mid-plane. Thus, $\langle V_\Phi \rangle$ at larger values of $|Z|$ could be slightly overestimated due to the selection effects.

3.3.3 Vertical component $\langle V_Z \rangle$

Figures 8 and 9 show the maps of vertical bulk motion $\langle V_Z \rangle$. Similar to $\langle V_R \rangle$, $\langle V_Z \rangle$ approximately ranges from -15 to 15 km s^{-1}, again in agreement with the previous studies (Widrow et al. 2012; Williams et al. 2013; Carlin et al. 2013). However, the vertical bulk motions are more severely affected by the systematic errors in proper motions, and there are more bins where UCAC4 and PPMXL give discrepant values. Williams et al. (2013) and Carlin et al. (2013) have found that

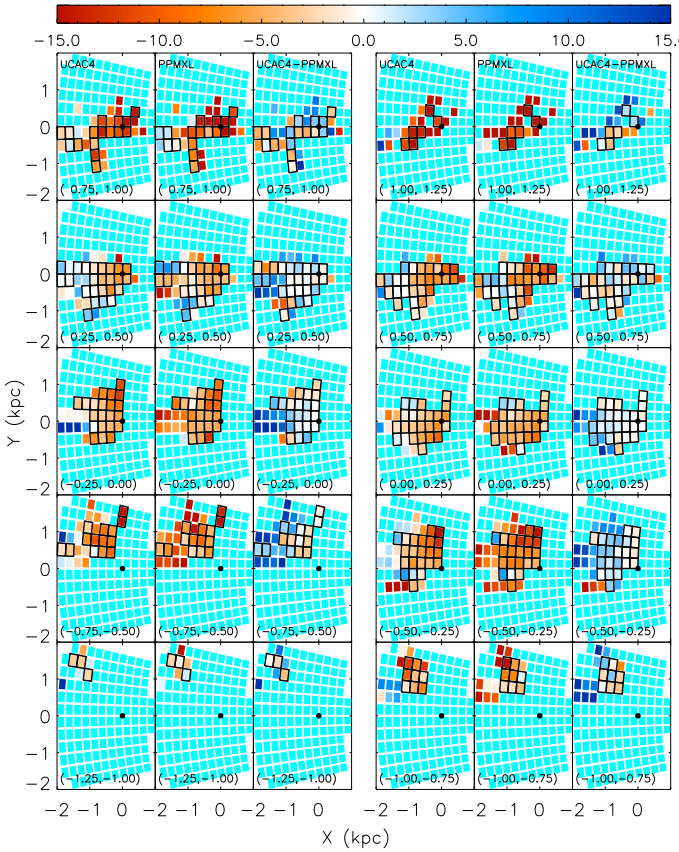

Fig. 6 Same as Fig. 4 but for $\langle V_\Phi \rangle - 220$ km s^{-1}.

the Galactic disk exterior to the solar position is compressing, i.e. stars above the mid-plane move downwards while those below move upwards. Our results confirm that the disk sector defined by $0 < \Phi < 6°$ is indeed compressing, but that of $-4 < \Phi < 0°$ is not. The UCAC4 results even show that the disk sector given by $-4 < \Phi < -2°$ is probably rarefying. Stars within $9 < R < 10$ kpc and $-2 < \Phi < 0°$, regardless if they are above or below the disk mid-plane, are found to be co-moving upwards, indicative of a bending-mode perturbation. More discussions on the vertical perturbations can be found in Section 3.5.

3.4 Giant Stellar Flows in the Disk

The bulk motion maps unveil spatially coherent, kpc-scale flows in the disk, as can be seen in Figures 10 and 11. At most locations, the UCAC4 and PPMXL proper motions give compatible results in terms of both speeds and directions.

Figure 10 displays $\langle V_R \rangle$ and $\langle V_Z \rangle$ as vectors in the R–Z plane. From $\Phi = -8°$ to $\Phi = -2°$, a giant flow, on a kpc scale with typical velocities $\sqrt{\langle V_R \rangle^2 + \langle V_Z \rangle^2} \gtrsim 10$ km s^{-1}, streams outwards and upwards from the solar neighborhood. The nearer parts of the flow ($R \leq 9$ kpc) become weaker in terms of typical velocity in the sector $-2 < \Phi < 0°$ and the direction is reversed between $\Phi = 0$

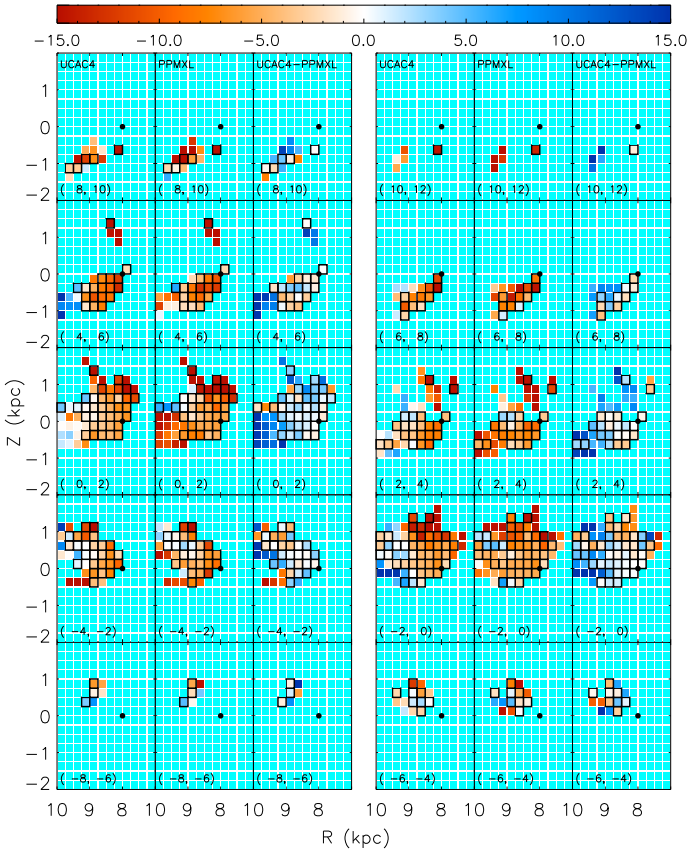

Fig. 7 Same as Fig. 5 but for $\langle V_\Phi \rangle - 220$ km s^{-1}.

and 2°: the flow now runs from outside into the solar neighborhood. For $\Phi > 2°$, we see the flow increases its speed back to $\gtrsim 10$ km s^{-1}, reaching a maximum of $\sim$20 km s^{-1}.

Figure 11, which plots $\langle V_R \rangle$ and $\langle V_\Phi \rangle - V_c$ in the X–Y plane, displays the giant flow from another perspective. Due to the large asymmetric drifts, the giant flow lags behind the circular motion by ≥ 10 km s^{-1} at $Z < -0.5$ kpc or $Z > 0.75$ kpc. Near the mid-plane, one sees an incomplete, clockwise vortex structure around $-1 < X < 0$ kpc and $-1 < Y < 0.5$ kpc. It has a diameter of $\sim$1 kpc and a typical velocity $\sqrt{\langle V_R \rangle^2 + (\langle V_\Phi \rangle - V_c)^2} \lesssim 10$ km s^{-1}. This structure is most obvious between $0 < Z < 0.5$ kpc.

3.5 Vertical Perturbations

The vertical kinematics has drawn considerable interest. Here we use $\langle V_Z \rangle (Z|R, \Phi)$ to denote the vertical bulk motion $\langle V_Z \rangle$ as a function of height Z at a specific location (R, Φ) in the disk plane. It has been shown that $\langle V_Z \rangle (Z|R, \Phi)$ can be decomposed into bending and breathing modes plus higher-order modes (Mathur 1990; Weinberg 1991; Widrow et al. 2014). The bending mode describes a situation where stars below and above the disk mid-plane move synchronously upwards or downwards, whereas the breathing mode refers to a scenario where stars below and above the mid-

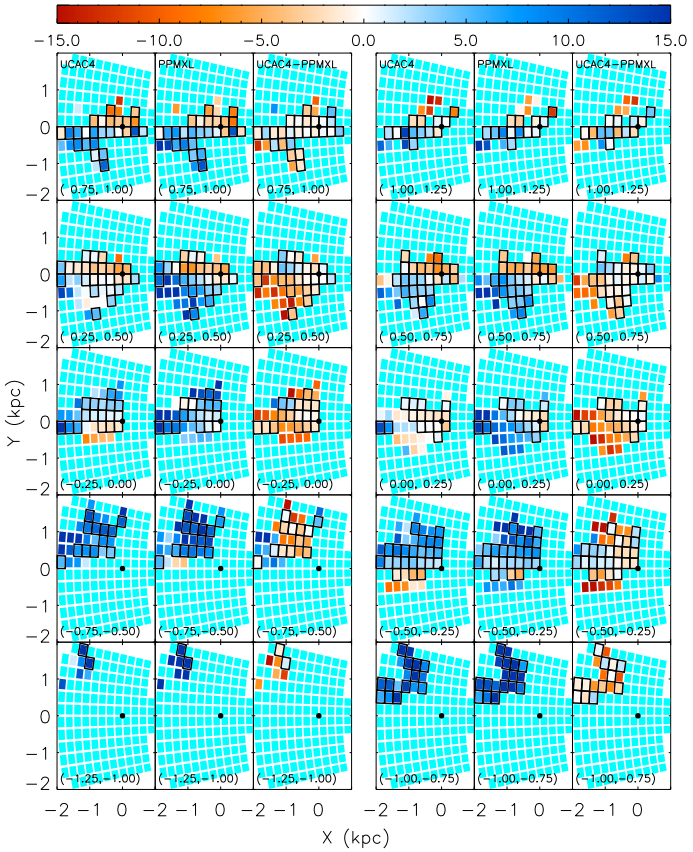

Fig. 8 Same as Fig. 4 but for $\langle V_Z \rangle$.

plane move in opposite vertical directions. The disk is said to be in compression when stars above the mid-plane move downwards and those below upwards, or in rarefaction vice versa.

To better display $\langle V_Z \rangle(Z|R, \Phi)$, we keep the bin size in the disk plane ΔR = 250 pc and $\Delta\Phi$ = 2° unchanged but increase the sampling frequency in height Z. Bins in Z are now spaced every 50 pc and have a height $Z \times 15\%$ (corresponding to the random errors) but no smaller than 100 pc. As before, $\langle V_Z \rangle$ is estimated by the median V_Z of stars in each bin. The curves of $\langle V_Z \rangle(Z|R, \Phi)$ are displayed in Figure 12 for cases where there are at least 10 data points and the range in heights spans at least 1 kpc.

3.5.1 Bending and breathing modes

Despite the complicated behavior of $\langle V_Z \rangle(Z|R, \Phi)$, we find that a simple linear fit can be applied to roughly describe their trends (see also Widrow et al. 2014), i.e.

$$\langle V_Z \rangle(Z \mid R, \Phi) = A(R, \Phi) \times Z + B(R, \Phi)\,, \tag{1}$$

where the intersection B, in units of km s^{-1}, parameterizes the bending mode (positive for upward and negative for downward co-movement) and the slope A, in units of km s^{-1} kpc^{-1}, parameterizes the breathing mode (positive for rarefaction and negative for compression).

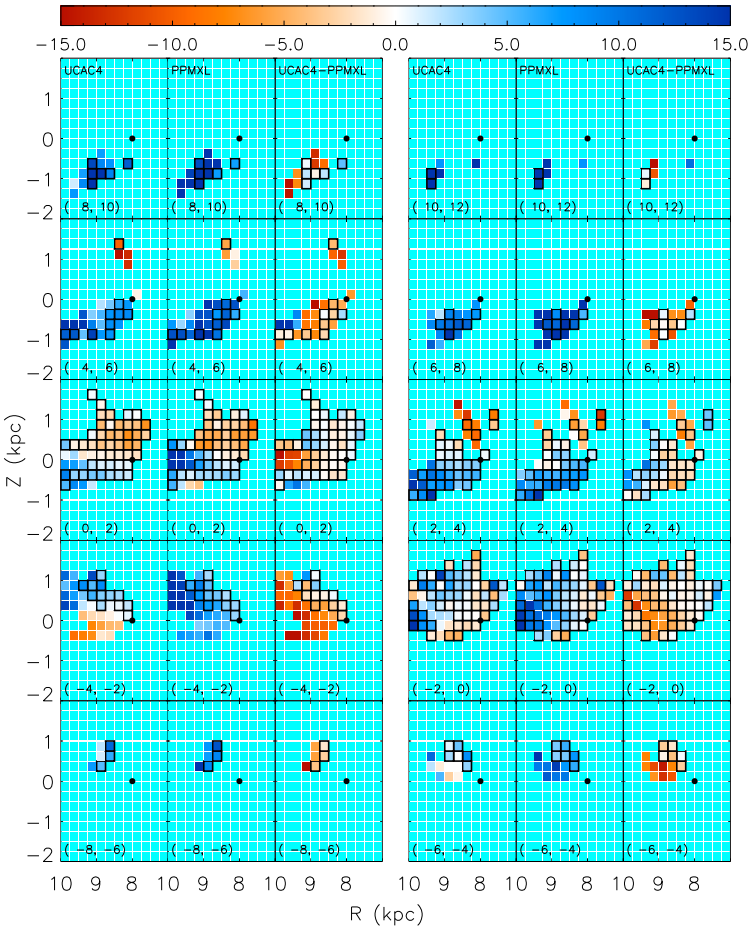

Fig. 9 Same as Fig. 5 but for $\langle V_Z \rangle$.

The distributions of the breathing-mode parameter A are displayed in Figure 13. The figure once again confirms the compression and rarefaction patterns already described in Section 3.3.3 but denoted here by reddish and blueish cells. Typical values of A range from $\sim$−15 km s^{-1} kpc^{-1} to $\sim$15 km s^{-1} kpc^{-1} (with the UCAC4 proper motions) or to $\sim$0 km s^{-1} kpc^{-1} (with the PPMXL proper motions). Out of 26 cells in total, 18 have the UCAC4 or PPMXL results consistent with each other within 5 km s^{-1} kpc^{-1}. Results from both sets of proper motions reveal a smooth, gradual change of A on kpc scales across the disk plane. The gradient is estimated to be roughly 18 km s^{-1} kpc^{-2}.

Figure 14 shows the distribution of bending mode parameter B, also found to possess smooth spatial variations. In the case of UCAC4 proper motions, the Galactic disk is found to have both upward and downward bending modes. However, with the PPMXL proper motions, we found that almost the whole region investigated has only an upward bending mode, except for one cell in the solar vicinity with B $\sim$−5 km s^{-1}. Still, more than two thirds of the cells have the UCAC4 or PPMXL results consistent with each other within 5 km s^{-1}. A gradient of $\sim$15 km s^{-1} kpc^{-1} is estimated for the bending mode parameter.

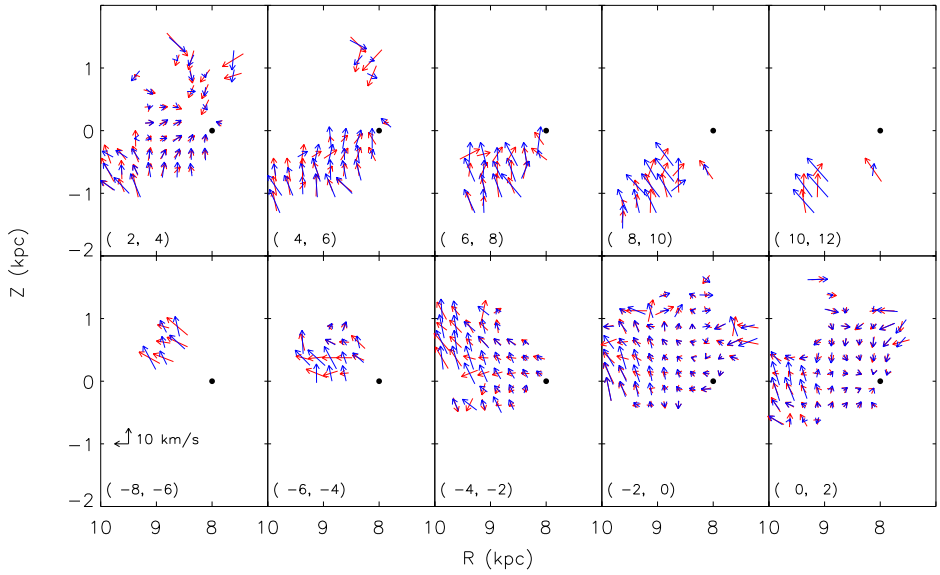

Fig. 10 Distributions of the magnitude and direction of the total velocity $\sqrt{\langle V_R\rangle^2 + \langle V_Z\rangle^2}$ in the R–Z plane. The arrows indicate the flow directions and their lengths are proportional to the total velocities. Red arrows are calculated with the UCAC4 proper motions, whereas those in blue are results from the PPMXL. Numbers in the brackets show the ranges of Φ in units of degrees. The black dots denote the location of the Sun.

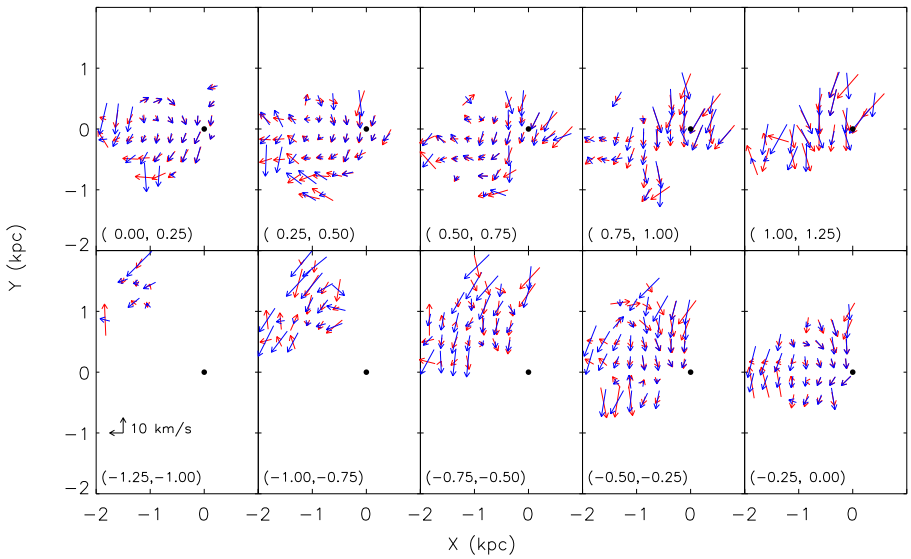

Fig. 11 Same as Fig. 10 but for the total velocity $\sqrt{\langle V_R\rangle^2 + (\langle V_\Phi\rangle - V_c)^2}$ in the X–Y plane. Numbers in the brackets show the ranges of Z in units of kpc.

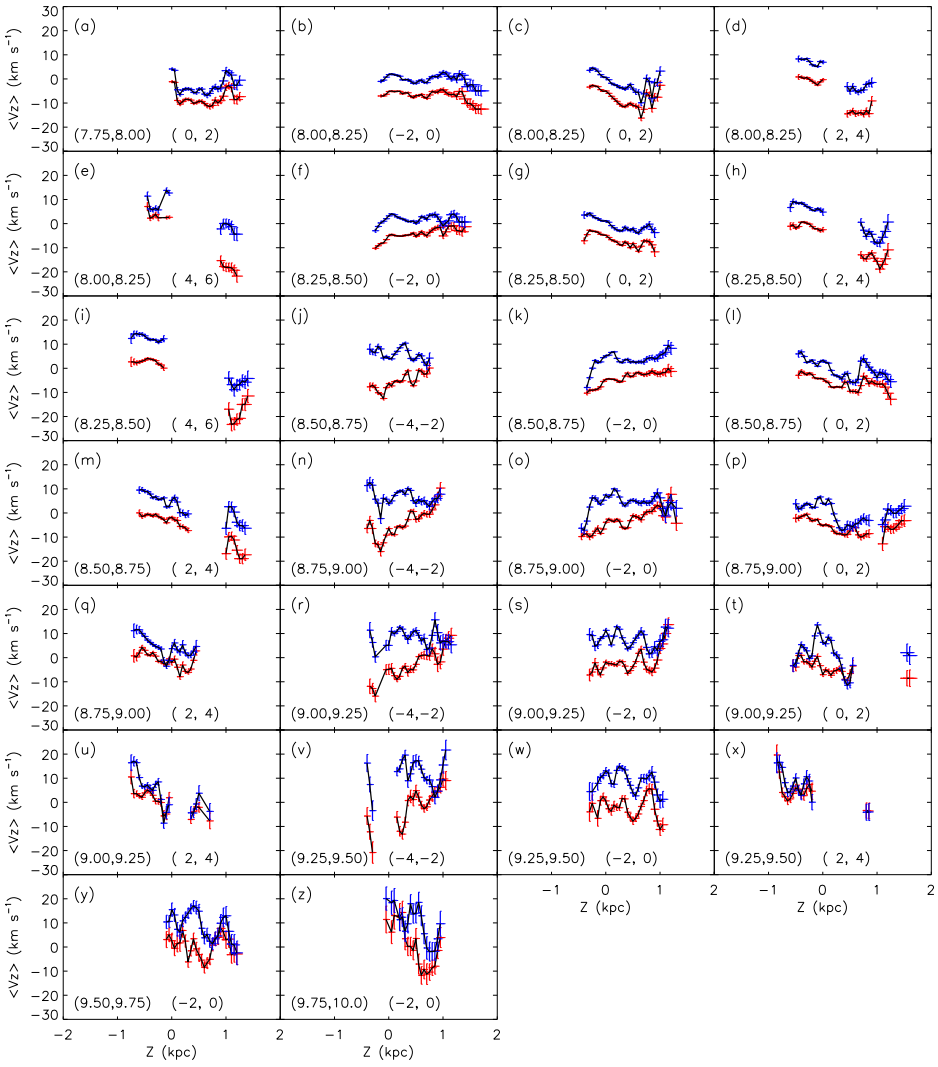

Fig. 12 Profiles of $\langle V_Z \rangle$ as a function of Z. In each panel, numbers in the parentheses on the left give the range of R in units of kpc, and the numbers in parentheses on the right that of Φ in units of degrees. Curves with red error bars have used the UCAC4 proper motions, while those with blue ones have used the PPMXL proper motions. The vertical error bars denote the 1σ random errors of $\langle V_Z \rangle$, whereas the horizontal ones are set to the bin size ΔZ. The UCAC4/PPMXL results have been shifted by $+/-5$ km s^{-1}, respectively, for clarity.

3.5.2 Breaks and ripples

In addition to the bending and breathing modes, the vertical bulk motion exhibits some higher-order perturbations, such as breaks or ripples along the $\langle V_Z \rangle (Z|R, \Phi)$ curves. A representative example of the breaks can be seen in Panel (l) of Figure 12 ($8.5\,\mathrm{kpc} < R < 8.75\,\mathrm{kpc}$, $0 < \Phi < 2^\circ$). $\langle V_Z \rangle$ first decreases smoothly from $Z = -0.5$ kpc to $Z = 0.6$ kpc, after which it jumps sharply by $\sim$10 km s^{-1}

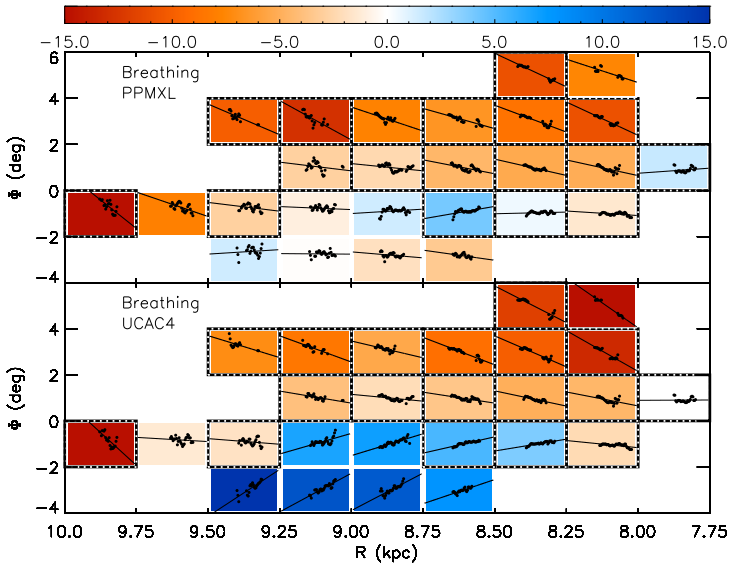

Fig. 13 Breathing mode parameter A in units of km s^{-1} kpc^{-1} (color scale) derived with the UCAC4 (*lower panel*) or the PPMXL (*upper panel*) proper motions. Each sub-panel plots $\langle V_Z \rangle$ as a function of Z (*points*) along with a linear fit to the data (*straight line*). The horizontal axis of each sub-panel ranges from -2 to 2 kpc and the vertical axis from -30 km s^{-1} to 30 km s^{-1}. Sub-panels enclosed in dotted black boxes show bins where the differences in A yielded by the UCAC4 and PPMXL proper motions differ by less than 5 km s^{-1} kpc^{-1}.

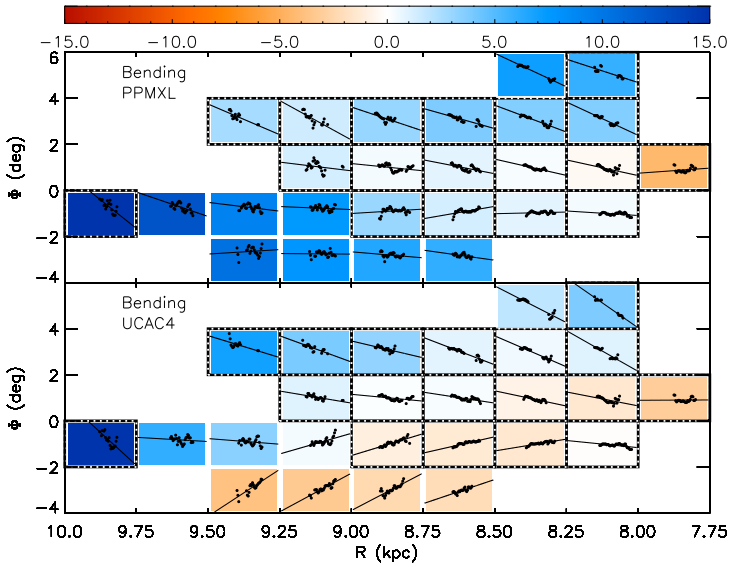

Fig. 14 Same as Fig. 13 but for bending mode parameter B in units of km s^{-1}. Sub-panels enclosed in dotted black boxes show bins where the UCAC4 and PPMXL values of B from UCAC4 and PPMXL differ by less than 5 km s^{-1}.

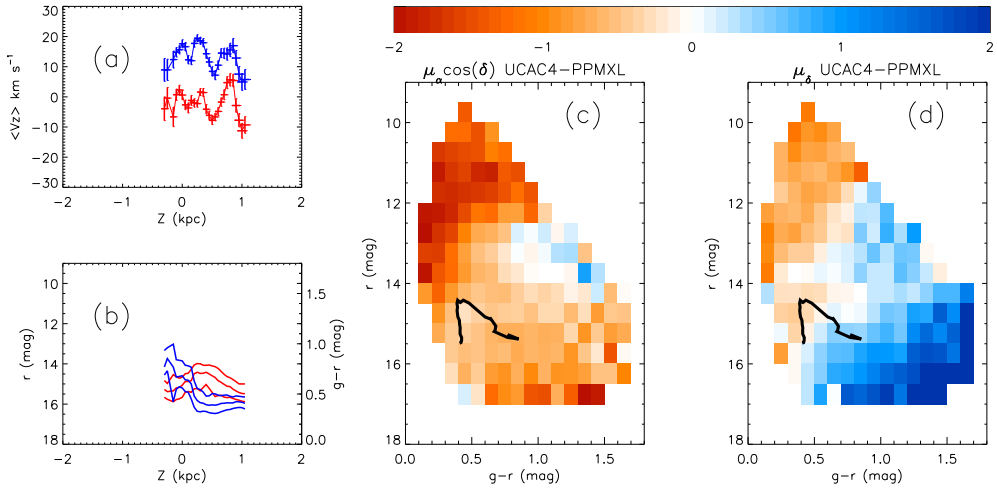

Fig. 15 Panel (a): $\langle V_Z \rangle$ as a function of Z for $9.25 < R < 9.5$ kpc and $-2 < \Phi < 0°$, same as for Panel (w) of Fig. 12. Panel (b): Distribution of $g - r$ colors (*blue curves*) and r magnitudes (*red curves*) as a function of Z, where the central lines denote the median values of $g - r$ or r and 25% of stars have values above/below the upper/lower lines. Panels (c, d): Locus of the median values of $g - r$ and r in the $(g - r, r)$ Hess diagram. The color scale denotes the median differences between the UCAC4 and PPMXL proper motions, the same as the color scale in Fig. 1.

within 0.2 kpc and then comes back again to a smooth gradual decrease with Z at $Z > 0.8$ kpc. The entire curve is broken by the two turning points at Z = 0.6 and 0.8 kpc into three segments, each well approximated by a linear function. Similar breaks can also be found in Panels (a, c, f).

The second kind of higher-order perturbation is characterized by high-frequency ripples in the $\langle V_Z \rangle (Z|R, \Phi)$ curves, especially at large distances from the Sun, e.g. panels (o-z) of Figure 12. The ripples have peak-to-peak amplitudes $A_{\rm pp}$ up to $\sim$10 km s^{-1} and frequencies k_Z of roughly 2–5 kpc^{-1}. Similar ripples have been found by Widrow et al. (2012), with comparable peak-to-peak amplitudes and frequencies. One may question whether these ripples arise from the unaccounted for color- and magnitude-dependent systematic errors in the proper motions. However, we believe that those ripples are probably real, as the color and magnitude distributions of stars vary smoothly with Z. An example is given in Figure 15, which shows the distributions of $g - r$ colors and r-band magnitudes of stars defined by $9.25 < R < 9.5$ kpc and $-2 < \Phi < 2°$ (corresponding to panel (w) of Fig. 12). It can be seen that both $g - r$ and r vary smoothly with Z, with no clear features corresponding to the peaks or dips of $\langle V_Z \rangle$ at Z = 0, 0.1, 0.3, 0.5 or 0.8 kpc. A small feature in $g - r$ at $Z = -0.2$ kpc is possibly related to a small dip at the same location in $\langle V_Z \rangle$ obtained with the UCAC4 proper motions. Moreover, the locus of $g - r$ and r median values in the $(g - r, r)$ Hess diagram occupies a region where the differences in $\mu_\alpha \cos\delta$ between UCAC4 and PPMXL are almost constant while the differences in μ_δ vary smoothly from 3 to -2 mas yr^{-1}. Although we do not know the systematic errors in UCAC4 or PPMXL proper motions themselves (we only know their differences), it is unlikely that they all vary quickly along the locus while at the same time generating smoothly varying differences. Thus it seems to us that the systematic errors in proper motions may not be responsible for the observed high-frequency ripples along the $\langle V_Z \rangle (Z|R, \Phi)$ curves.

4 BULK MOTIONS OF THE LOCAL STELLAR POPULATIONS

It is an interesting problem whether different stellar populations share the same bulk motions. Smith et al. (2012) and Widrow et al. (2012) show that there are differences of up to $\sim$5 km s^{-1} between stars with different metallicities or colors. Such a study is not feasible for the global sample, as the potential color-dependent systematic errors in proper motions may generate false bulk motion differences among populations with different colors, especially at large distances. We thus restrict ourselves to the local sample, which contains 5443 FGK stars with distances $\leq$ 150 pc from the Sun (see Sect. 2.3.2). At this distance limit, a 1 mas yr^{-1} error in the proper motion corresponds to a $\sim$0.7 km s^{-1} error in the tangential velocity perpendicular to the line of sight.

The local sample is divided into a metal-rich group ([Fe/H] > -0.4 dex) and a metal-poor group ([Fe/H] < -0.4 dex). Each of the two groups is further divided into three based on the spectral types, the F-type ($6000 < T_{\rm eff} < 6800$ K), G-type ($5000 < T_{\rm eff} < 6000$ K) and K-type ($4200 < T_{\rm eff} < 5000$ K). $\langle V_R \rangle$, $\langle V_\Phi \rangle$ and $\langle V_Z \rangle$ are estimated by the median velocities of stars in each population, and the results can be found in Table 1 and Figure 16.

The differences between UCAC4 and PPMXL results for each population are smaller than $\sim$1 km s^{-1}, or within the random errors. However, the differences between different populations, either in $\langle V_R \rangle$, $\langle V_\Phi \rangle$ or $\langle V_Z \rangle$, are well beyond the errors at high levels of significance. The variations of azimuthal bulk motions are the most obvious, with $\langle V_\Phi \rangle -$ 220 km s^{-1} ranging from $\sim$2 km s^{-1} for the metal-rich F-type stars to ~ -20 km s^{-1} for the metal-poor K-type stars. This is expected, considering the larger velocity dispersions and asymmetric drifts of older stars. From F-type to K-type, $\langle V_R \rangle$ steadily increases from $\sim$0 to $\sim$4 km s^{-1} for the metal-rich populations, or from ~ -6 km s^{-1} to $\sim$2 km s^{-1} for the metal-poor populations. For each spectral type, the metal-poor stars always have lower values of $\langle V_R \rangle$ than the metal-rich ones. Similarly, $\langle V_Z \rangle$ decreases towards later spectral types among the metal-rich populations, from $\sim$2 km s^{-1} for the F-type stars to ~ -2 km s^{-1} for the K-type stars. For the metal-poor populations, values of $\langle V_Z \rangle$ of the G-type stars are lower than those of the F-type by $\sim$3 km s^{-1}, but almost equal to those of the K-type. For each spectral type, metal-poor stars always have larger $\langle V_Z \rangle$ than metal-rich ones.

5 VELOCITY STRUCTURES IN THE GALACTIC ANTI-CENTER

Stars along the path from the Sun towards the Galactic Anti-center have Galactocentric radial velocities V_R aligned with their line-of-sight radial velocities V_r. With an analysis of the line-of-sight radial velocities of $\sim$700 RC stars in the direction of the Galactic Anti-center, Liu et al. (2012) report a "velocity bifurcation" at Galactocentric radii 10–11 kpc and attribute it to a resonance feature of the central bar. However, since the majority of stars in their sample fall just around these radii, it is thus possible that the bifurcation may not be a localized feature but rather a global one – it was only detected at these radii simply because of the limited distance range probed by the sample.

To clarify the situation, we make use of the anti-center sample defined in Section 2.3.3, consisting of 1716 GK-, 1402 F-, 359 A-type dwarfs and 958 RC giants. Their distance distributions can be found in panels (a–d) of Figure 17. With increasing luminosities, the four groups of stars are able to trace a contiguous distance range from the solar vicinity of $R \sim$8 kpc out to $R \sim$12 kpc.

Panels (e–i) show the stellar number density distributions of the anti-center sample in the (R, V_r) plane. The distributions exhibit a rich variety of velocity structures at different distance regimes. In the first regime, 8.0–8.6 kpc, there are four concentrations of GK-type dwarfs at $V_r \sim -32$, -15, 0 and 18 km s^{-1}, respectively. They are apparently related to the known moving groups: the -32 km s^{-1} concentration is linked with Wolf 630, the -15 km s^{-1} one with Sirius, the 0 km s^{-1} one with Coma Berenices, and the concentration at 18 km s^{-1} comes from the Pleiades (see e.g. Dehnen 1998; Antoja et al. 2012). Moving out to the 8.6–9.0 kpc regime, however, the F-type dwarfs only show two peaks at $V_r \sim -30$ and -5 km s^{-1}, respectively. In the third regime, 9.0–9.5 kpc, there is a single concentration of A-type dwarfs at $V_r \sim -10$ km s^{-1}. Then the concentration moves

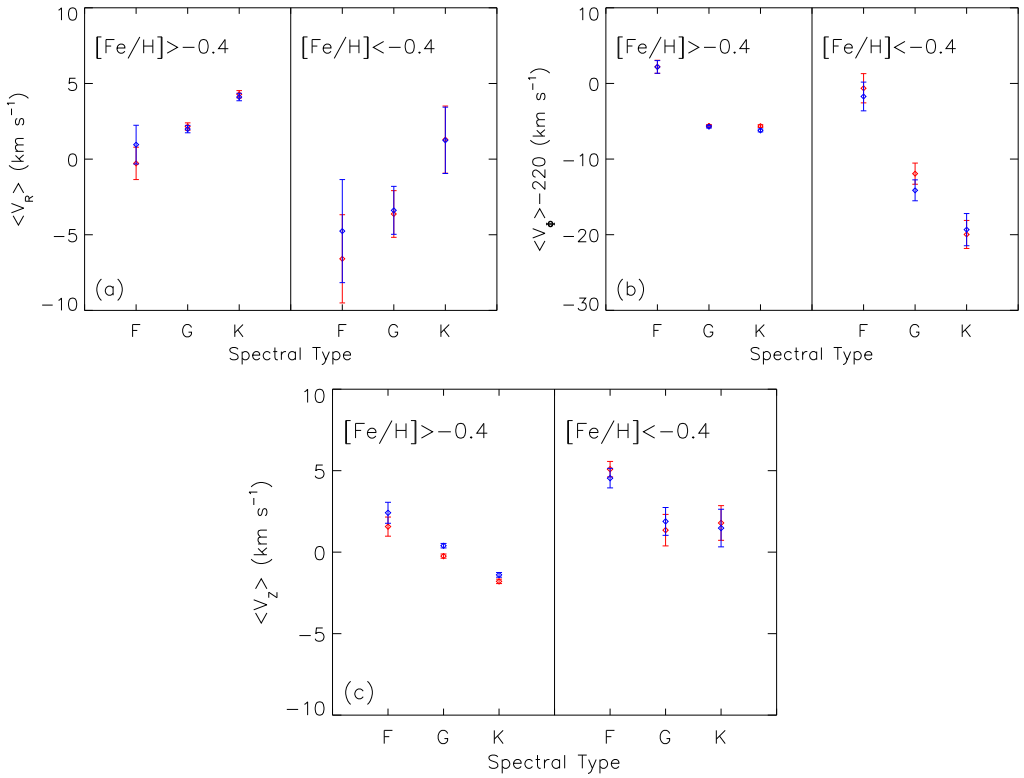

Fig. 16 $\langle V_R \rangle$, $\langle V_\Phi \rangle$ and $\langle V_Z \rangle$ for different populations of the local sample. The red symbols are calculated with the UCAC4 proper motions while those in blue with the PPMXL values.

to V_r ∼0 km s^{-1} between 9.5–10 kpc traced by RC stars. In the regime of 10–11 kpc, the "velocity bifurcation" reported by Liu et al. (2012) is clearly visible, appearing as two stellar concentrations at V_r ∼20 and −10 km s^{-1}, respectively. The peaking velocities are slightly lower than theirs, by ∼6 km s^{-1}, which possibly originates from the measurement uncertainties. Further out to 11–12 kpc, the RC giants show a new triple-peaked structure, with peaks located at V_r ∼5 km s^{-1}, 20 km s^{-1} and 35 km s^{-1}, respectively.

Antoja et al. (2012) have investigated the moving groups in different regions of the disk, showing that they drift in velocity space at different radii. Similarly, the anti-center sample reveals contiguous spatial variations of velocity structures, from the solar vicinity out to R = 12 kpc. Specifically, the anti-center sample analyzed here shows that while the "velocity bifurcation" reported by Liu et al. (2012) is indeed a localized feature, it is also not the sole feature in the direction of the Galactic Anti-center. It is thus not an obvious conclusion that the "velocity bifurcation" is a resonance feature of the central bar, and the formation mechanisms of these features need further investigations.

6 SUMMARY

In this paper we have carried out a detailed investigation of bulk motions of the nearby Galactic stellar disk using three samples selected from the LSS-GAC DR2: a global sample of ∼0.57 million FGK dwarfs out to a distance of ∼2 kpc, a local sample of ∼5400 FGK dwarfs with distances

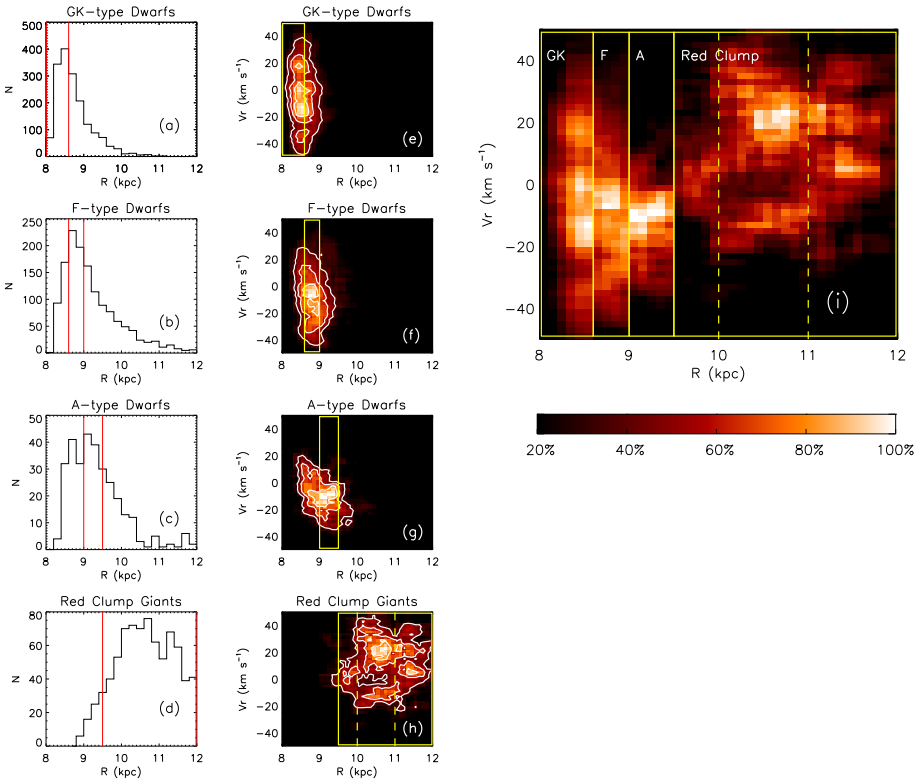

Fig. 17 Panels (a–d): Distributions of Galactocentric distances of GK-, F- and A-type dwarfs and RC giants in the anti-center sample. The red lines in the four panels mark the distance ranges of the boxed regions in Panels (e–h), respectively. Panels (e–h): Stellar number density distributions of the four populations in the (R, V_r) plane. The color scale is proportional to the number of stars in a 500 pc $\times$ 10 km s^{-1} running box relative to the maximum. The white lines are the corresponding 40%, 60% and 80% contours from outside to inside. Panel (i): Mosaic of the boxed regions in Panels (e–h). The yellow dashed lines and boxes mark the boundaries of distance regimes mentioned in Sect. 5.

$\leq$ 150 pc, and an anti-center sample containing $\sim$4400 AFGK dwarfs and RC giants extending out to $\sim$4 kpc in the direction of the Galactic Anti-center.

With the global sample, we have provided a three-dimensional map of bulk motions of the Galactic disk from the solar vicinity out to $\sim$2 kpc with a spatial resolution of $\sim$250 pc. Typical values of radial and vertical bulk motions range from -15 to 15 km s^{-1}, while the lag behind the circular motion dominates the azimuthal bulk motion by up to $\sim$15 km s^{-1}. The map reveals spatially coherent, kpc-scale stellar flows, with typical velocities of a few tens km s^{-1}. We have analyzed the bending and breathing modes and higher-order perturbations. The bending and breathing modes are clearly visible, and vary smoothly across the disk plane. The data also reveal breaks and ripples in the profiles of vertical bulk motion versus height, indicative of higher-order perturbations.

With the local sample, we have studied the bulk motions of different stellar populations. Differences of several km s^{-1} are found in the radial and vertical bulk motions, while the azimuthal bulk motions exhibit larger differences.

The anti-center sample reveals abundant velocity structures at distances ranging from the solar vicinity out to a Galactocentric radius of 12 kpc, with the nearer ones apparently related to the known

moving groups. The "velocity bifurcation" reported by Liu et al. is confirmed to be a localized feature at 10–11 kpc, beyond which the data reveal a new triple-peaked structure.

Acknowledgements This work is supported by the National Key Basic Research Program of China (2014CB845700). This work has used data products from the Guo Shou Jing Telescope (the Large Sky Area Multi-Object Fiber Spectroscopic Telescope, LAMOST). LAMOST is a National Major Scientific Project built by the Chinese Academy of Sciences. Funding for the project has been provided by the National Development and Reform Commission. LAMOST is operated and managed by National Astronomical Observatories, Chinese Academy of Sciences.

References

Antoja, T., Helmi, A., Bienayme, O., et al. 2012, MNRAS, 426, L1
Bovy, J., Bird, J. C., García Pérez, A. E., et al. 2015, ApJ, 800, 83
Bressan, A., Marigo, P., Girardi, L., et al. 2012, MNRAS, 427, 127
Carlin, J. L., DeLaunay, J., Newberg, H. J., et al. 2013, ApJ, 777, L5
Cui, X.-Q., Zhao, Y.-H., Chu, Y.-Q., et al. 2012, RAA (Research in Astronomy and Astrophysics), 12, 1197
Debattista, V. P. 2014, MNRAS, 443, L1
Dehnen, W. 1998, AJ, 115, 2384
Eisenstein, D. J., Weinberg, D. H., Agol, E., et al. 2011, AJ, 142, 72
Faure, C., Siebert, A., & Famaey, B. 2014, MNRAS, 440, 2564
Huang, Y., Liu, X.-W., Yuan, H.-B., et al. 2015a, MNRAS, 449, 162
Huang, Y., Liu, X.-W., Zhang, H.-W., et al. 2015b, RAA (Research in Astronomy and Astrophysics), 15, 1240
Liu, C., Xue, X., Fang, M., et al. 2012, ApJ, 753, L24
Liu, X.-W., Yuan, H.-B., Huo, Z.-Y., et al. 2014, in IAU Symposium, 298, eds. S. Feltzing, G. Zhao, N. A. Walton, & P. Whitelock, 310
Liu, X. W., Zhao, G., & Hou, J. L. 2015, RAA (Research in Astronomy and Astrophysics), 15, 1089
Massa, D., Savage, B. D., & Fitzpatrick, E. L. 1983, ApJ, 266, 662
Mathur, S. D. 1990, MNRAS, 243, 529
Nordström, B., Mayor, M., Andersen, J., et al. 2004, A&A, 418, 989
Roeser, S., Demleitner, M., & Schilbach, E. 2010, AJ, 139, 2440
Schönrich, R., & Binney, J. 2012, MNRAS, 419, 1546
Schwarzschild, K., & Villiger, W. 1907, Astronomische Nachrichten, 174, 133
Siebert, A., Famaey, B., Minchev, I., et al. 2011, MNRAS, 412, 2026
Smith, M. C., Whiteoak, S. H., & Evans, N. W. 2012, ApJ, 746, 181
Stecher, T. P. 1965, ApJ, 142, 1683
Steinmetz, M., Zwitter, T., Siebert, A., et al. 2006, AJ, 132, 1645
Weinberg, M. D. 1991, ApJ, 373, 391
Widrow, L. M., Gardner, S., Yanny, B., Dodelson, S., & Chen, H.-Y. 2012, ApJ, 750, L41
Widrow, L. M., Barber, J., Chequers, M. H., & Cheng, E. 2014, MNRAS, 440, 1971
Williams, M. E. K., Steinmetz, M., Binney, J., et al. 2013, MNRAS, 436, 101
Xiang, M. S., Liu, X. W., Yuan, H. B., et al. 2015, MNRAS, 448, 822
Yanny, B., Rockosi, C., Newberg, H. J., et al. 2009, AJ, 137, 4377
Yuan, H. B., Liu, X. W., & Xiang, M. S. 2013, MNRAS, 430, 2188
Yuan, H.-B., Liu, X.-W., Huo, Z.-Y., et al. 2015, MNRAS, 448, 855
Zacharias, N., Finch, C. T., Girard, T. M., et al. 2013, AJ, 145, 44
Zhao, G., Zhao, Y.-H., Chu, Y.-Q., Jing, Y.-P., & Deng, L.-C. 2012, RAA (Research in Astronomy and Astrophysics), 12, 723